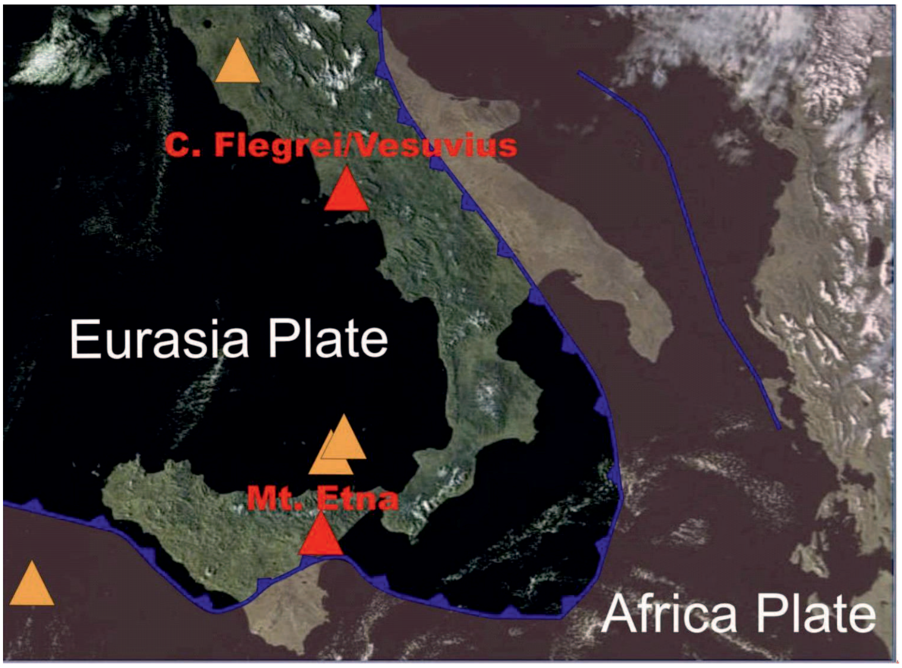

Figure 1
Geographical and geodynamic position of Mt. Etna and Campi Flegrei / Vesuvius Supersites.

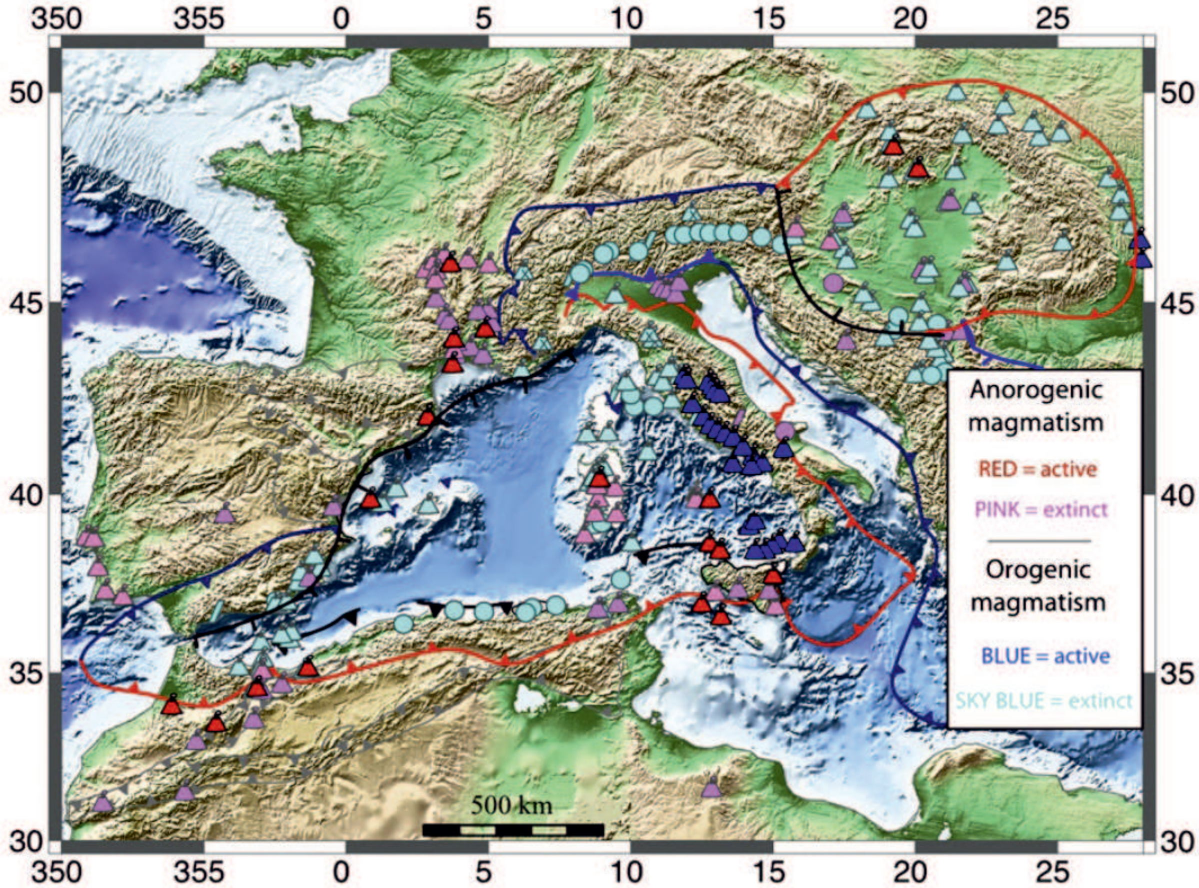

Figure 2
Distribution of Tertiary magmatism in the Central–Western Mediterranean region. Triangles: volcanics and pyroclastics; Triangles with crosses: volcanoclastics; Circles: plutons; Slashes: dykes. Red symbols: active “anorogenic” igneous rocks; Pink symbols: extinct “anorogenic” igneous rocks; Blue symbols: active “subduction-related” igneous rocks; Sky Blue symbols: fossil “subduction-related” igneous rocks (from Carminati, E., et al., Geodynamic evolution of the central and western Mediterranean: Tectonics vs. igneous petrology constraints, Tectonophysics (2012), doi:10.1016/j.tecto.2012.01.026.)

Figure 3
Two Version of the project logo: left, version of the MED-SUV logo until the end of FP7 program; right, version of the logo since 2014.

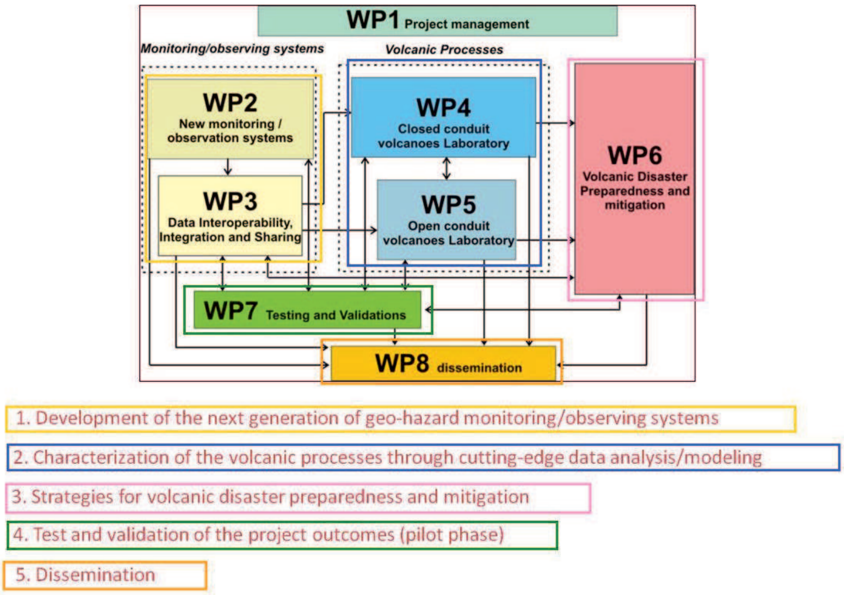

Figure 4
Objectives and work program of MED-SUV: Structure and functional links of the work pakages.

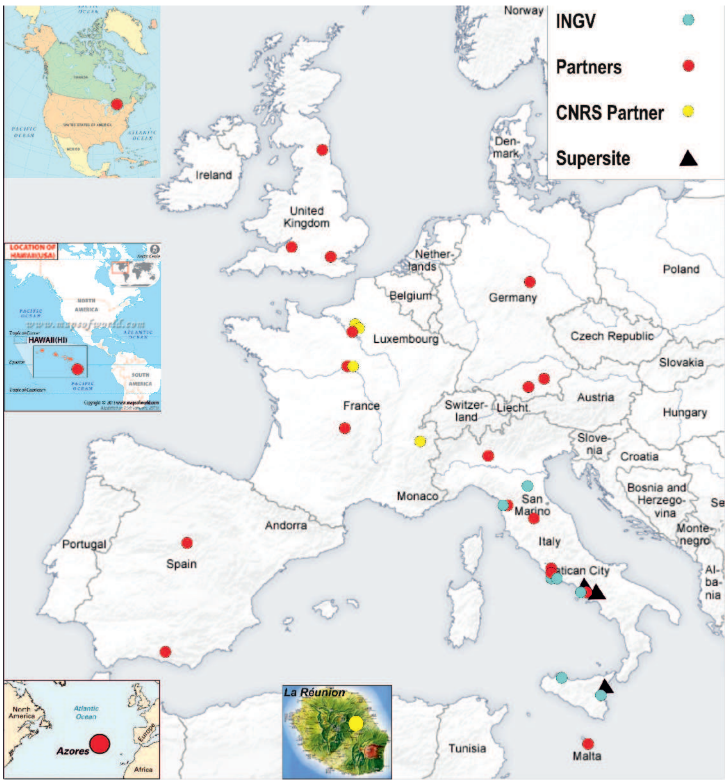

Figure 5
MEDiterranean Supersite Volcanoes (MED-SUV) Project Partners' geographic distribution

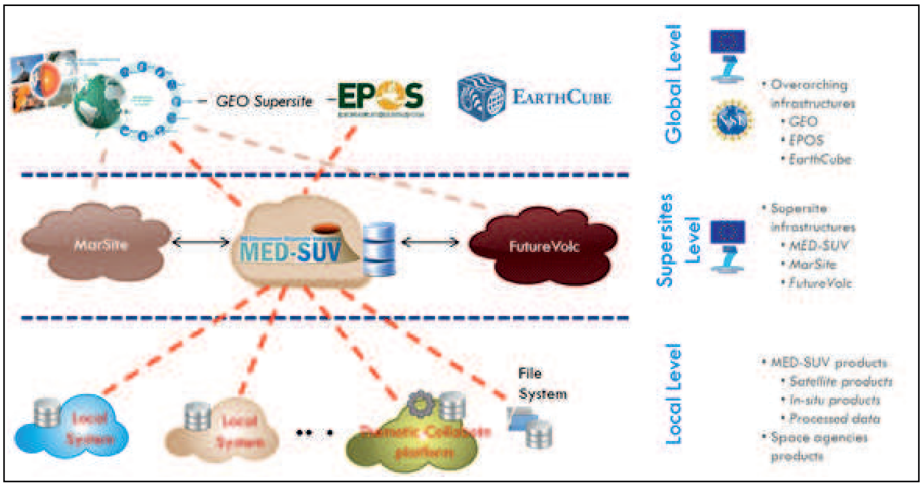

Figure 6

- General Architecture of MED-SUV e-Infrastructure (Mazzetti et al., in prep.).
- At the Local Level, the relevant datasets can be discovered and accessed through heterogeneous systems including: a) filesystems/databases storing datasets, b) data discovery and access services, c) collaboration platforms for processing and analytics.
- At the Supersite Level, aggregation of local systems is carried out. Supersite users are provided with harmonized discovery and access of local products.
- At the Global Level, overarching systems access the Supersites systems.

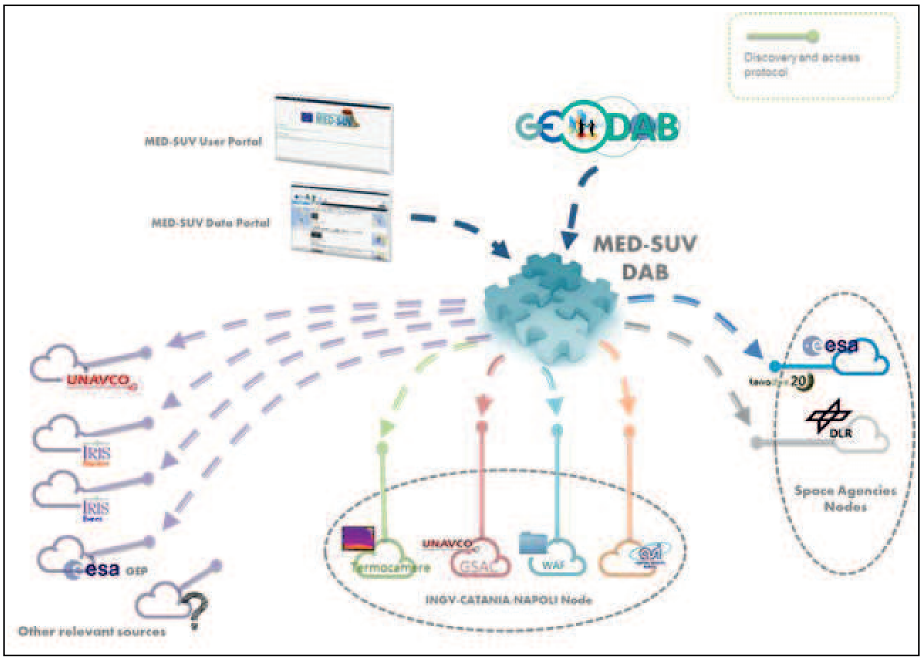

Figure 7
Current implementation of the MED-SUV logical architecture: Data Provider Services accessed by the DAB. The Local Level is represented by several data provider nodes: Space Agency repositories, the MED-SUV local repository managed by INGV and other relevant data sources (Mazzetti et al., in prep.).

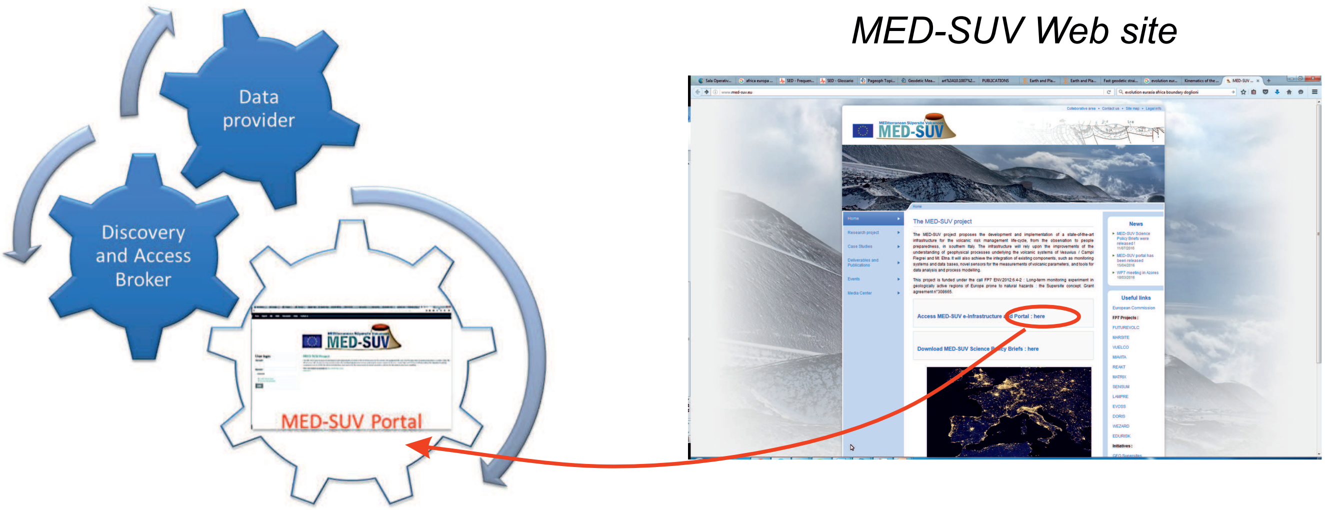

Figure 8
Functional architecture of the main elements of the MED-SUV e-Infrastructure. Users access to the portal (left) from the web site (right). The portal allows access to the data provider resources through the DAB.

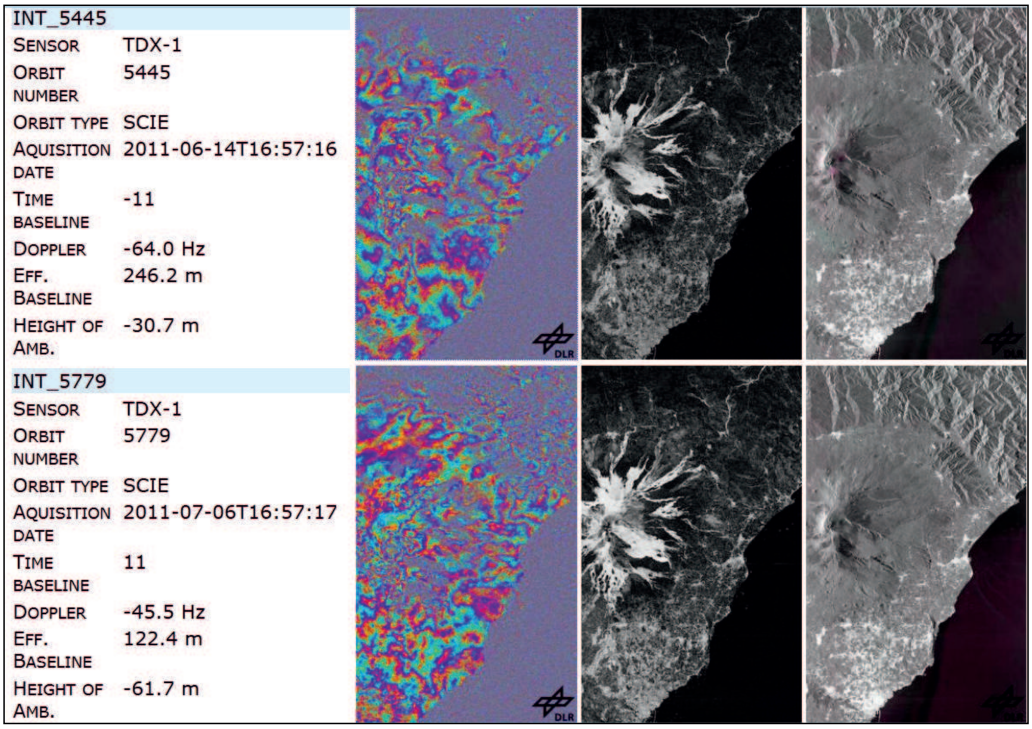

Figure 9
Example of IWAP products on Mt. Etna volcano. The images show the differential phase (left), differential coherence (middle) and amplitude colour composite (right) maps, which are automatically generated by the IWAP processor (courtesy of C. Minet; DLR copyright).

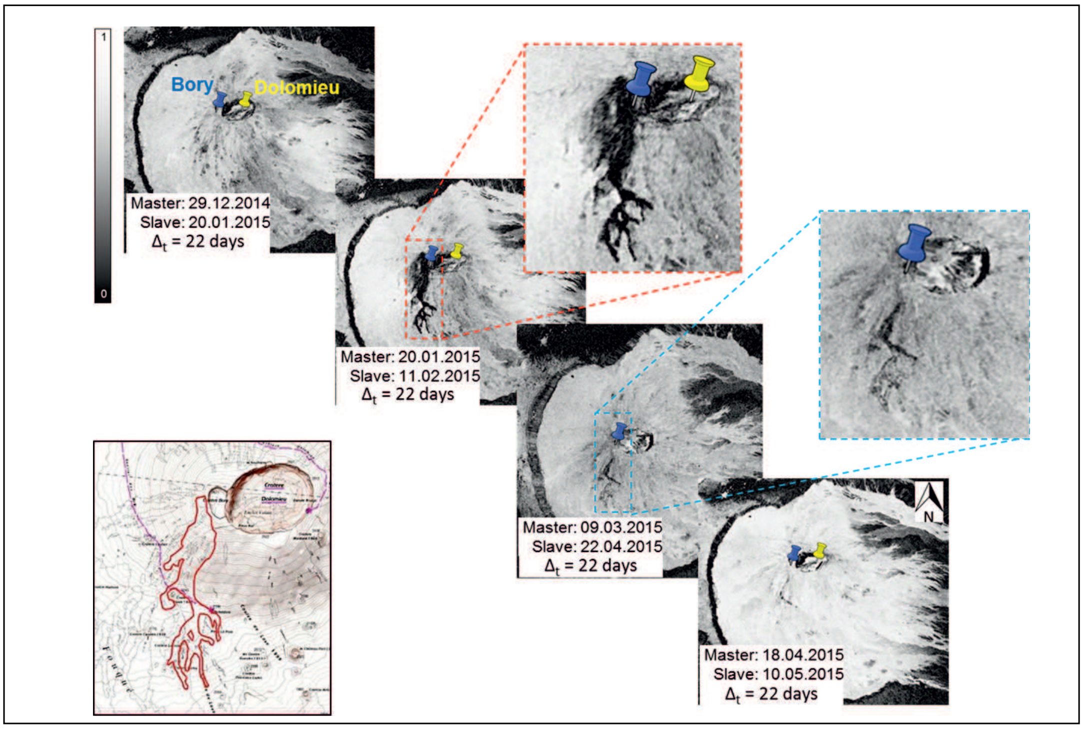

Figure 10
Example of IWAP products on Piton de la Fournaise volcano. The images show the differential coherence images inside the Enclos caldera corresponding to four different phases of the 2015 eruption (courtesy C. Minet; DLR copyright).

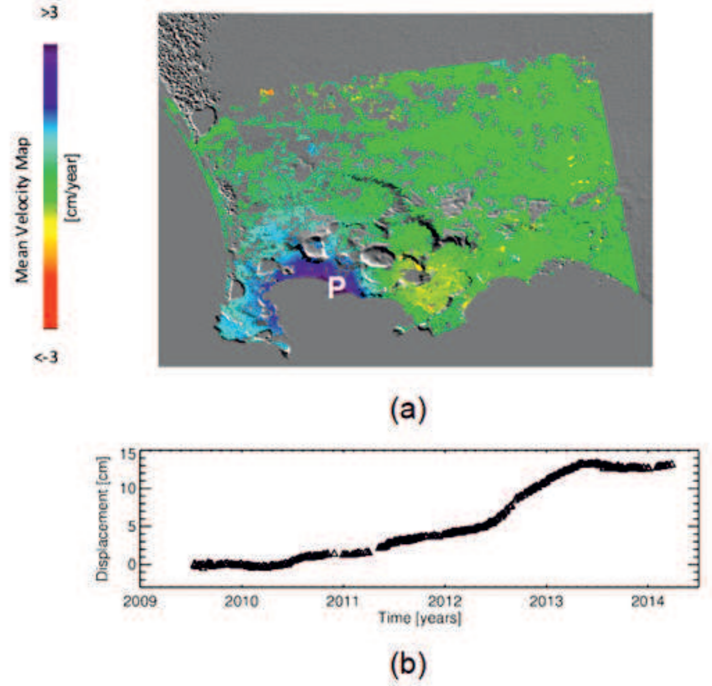

Figure 11
Examples of SBAS analysis for Campi Flegrei: (a) shows the Mean Displacement Velocity Map as retrieved using CSK Ascending SAR data set; (b) is the Time-Series of Deformation related to the pixel labelled as P in (a) located nearby the Pozzuoli Harbour (courtesy of A. Pepe; CNRS-IREA copyright).

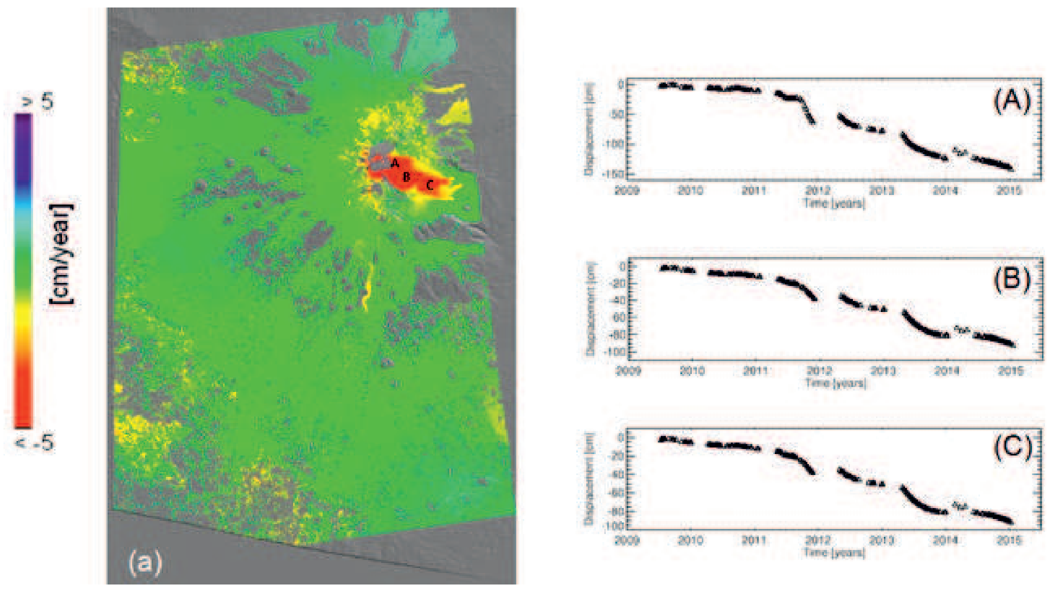

Figure 12
Examples of SBAS analysis for Mt. Etna CSK DInSAR results (ascending orbits); (a) shows the Mean Displacement Velocity Map; (A)-(C) Plot the deformation time-series corresponding to pixels labelled (A)-(C) located in the Valle del Bove area at varying distances from the summit crater (courtesy of A. Pepe; CNRS-IREA copyright).

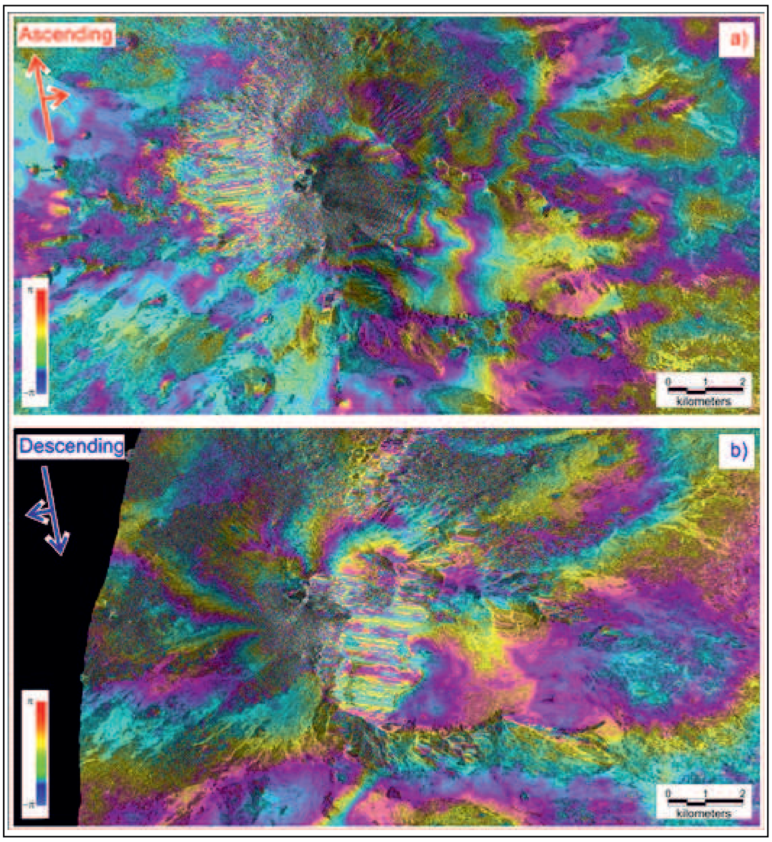

Figure 13
Example of uses of SAR for volcano monitoring. Differential interferograms relevant to the December 2014 Mt. Etna paroxysmal episodes. (a) ascending December 6, 2014 – January 8, 2015 SAR data pair and (b) descending December 26, 2014 – January 6, 2015 SAR data pair. (courtesy of F. Guglielmino; INGV copyright).

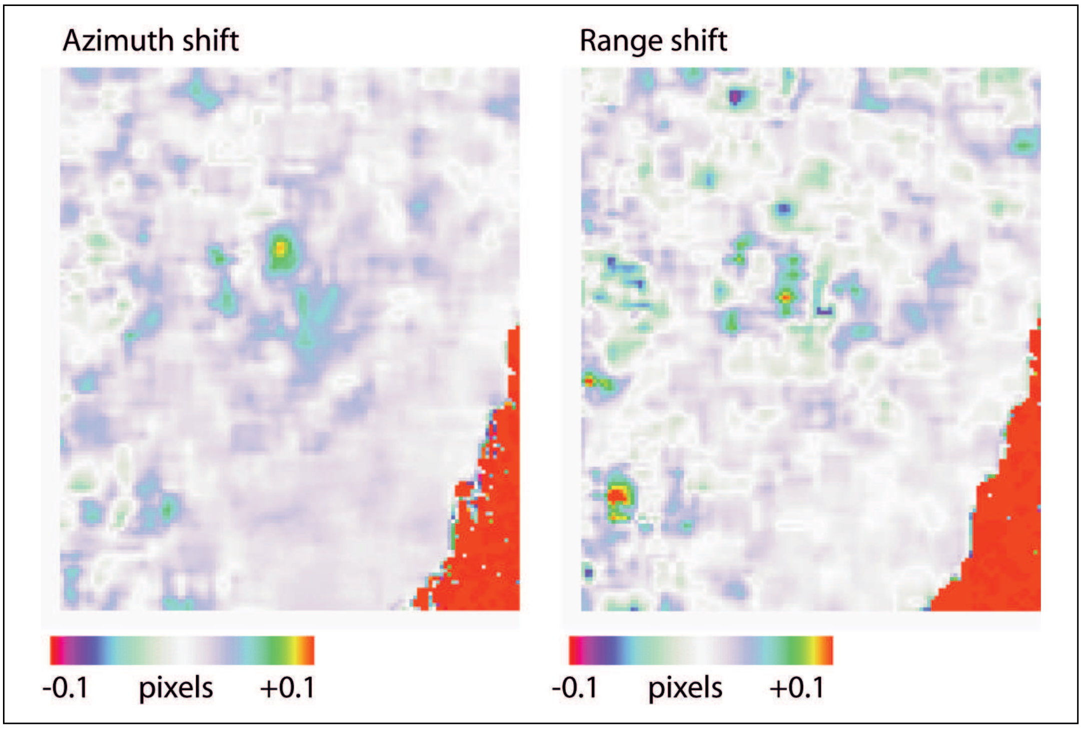

Figure 14
Example of uses of SAR for volcano monitoring. (B) Sub Aperture Offset Tracking method applied on Radarsat-2 data to detect volcanic plumes; there is a pixel offset anomaly located around the Etna summit (particularly visible in the azimuth shift) (courtesy of M. De Michele; BRGM copyright).

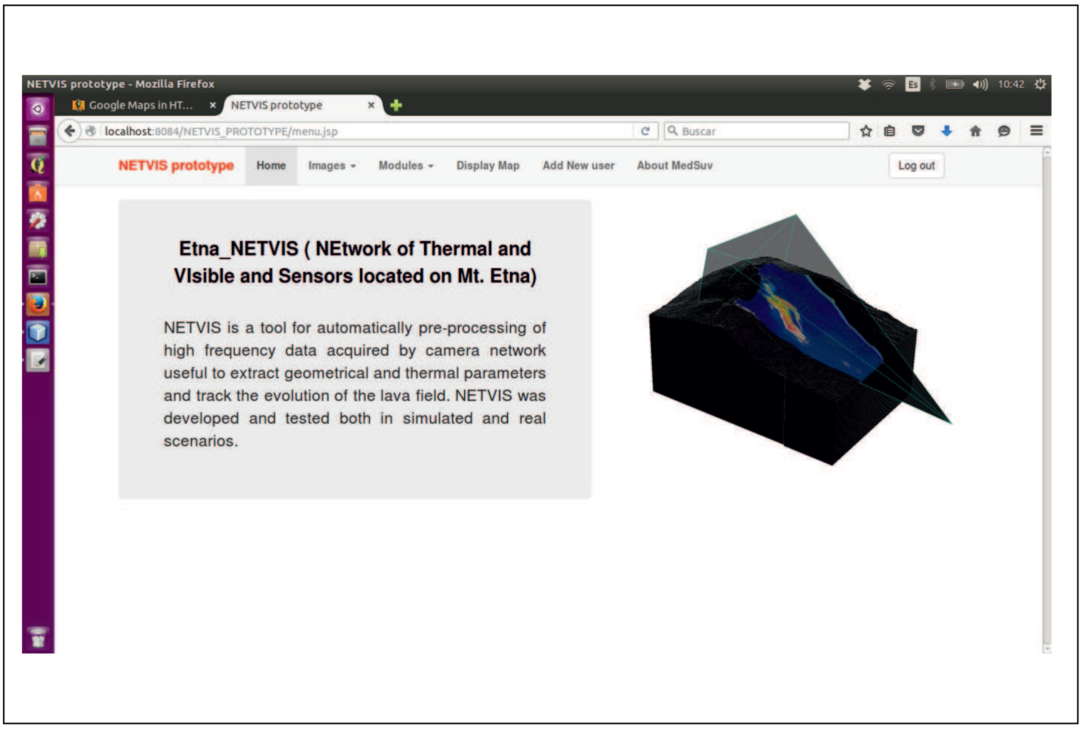

Figure 15. NETVIS tool interface

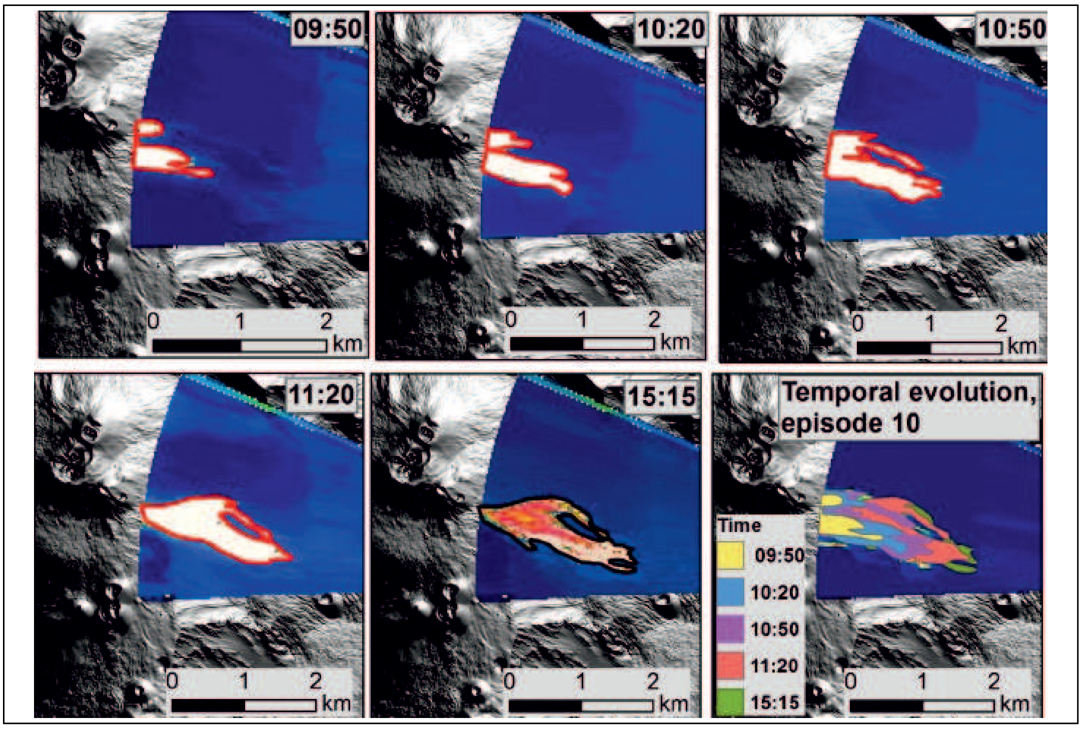

Figure 16
NETVIS application on Mt. Etna. Orthophotos extracted through the NETVIS tool from the Etna Monte Cagliato video-camera images of 12/08/2011, and delimitation of the lava flow field evolution (courtesy of M. Marsella; SurveyLab copyright).

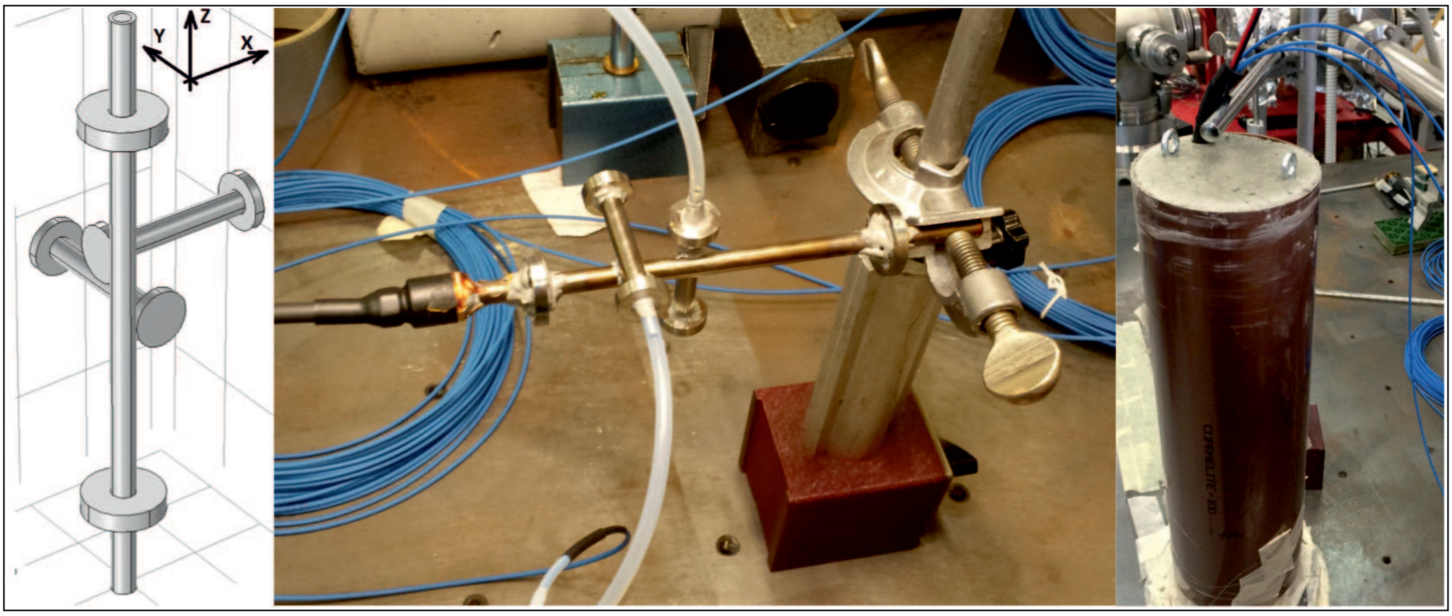

Figure 17.
FBG sensor and GILDA Data logger. The multi-axial strain sensor (Left: mechanical design; centre: multi-axis prototype; right: borehole system) (courtesy of F. Sorrentino; Marwan Copyright).

Figure 18
FBG sensor and GILDA Data logger. Site of the borehole installation on Mt. Etna (upper left); readout electronics box, including the GILDA data logger (upper right); the tri-axial strainmeter on the borehole (lower) (courtesy of F. Sorrentino; Marwan Copyright).

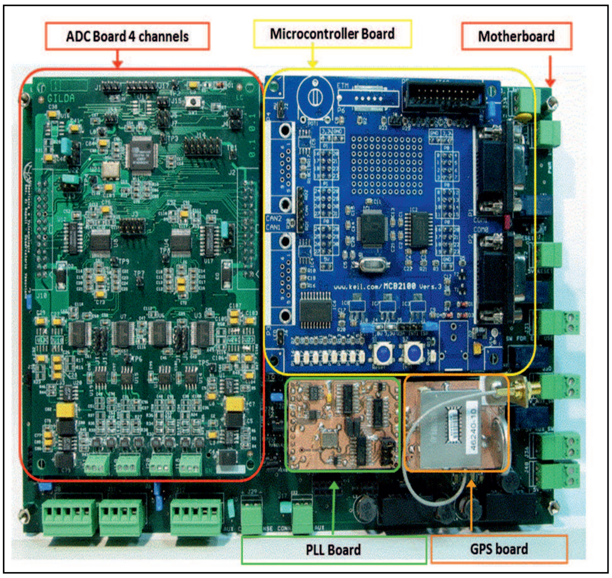

Figure 19
FBG sensor and GILDA Data logger. The detail of the GILDA data logger. (courtesy of F. Giudicepietro; INGV copyright).

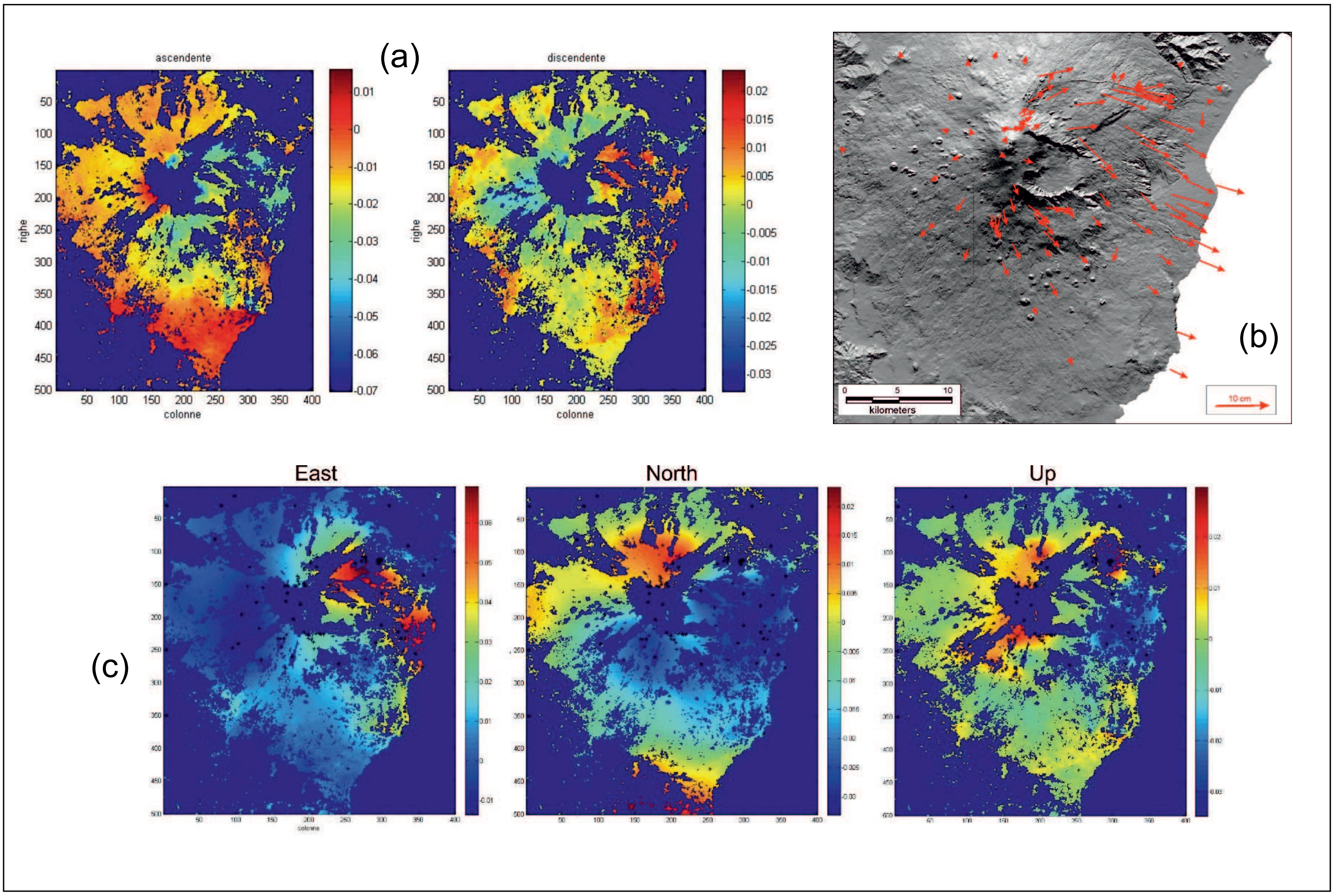

Figure 20
EO and in-situ ground deformation data integration through SISTEM. Example relevant to Mt. Etna 2009-2010 period: a) ENVISAT Line of Sight (LOS) mean velocity map (values are in m/yr); (b) GPS horizontal displacement vectors; (c) the three components of the displacement resulting from the application of SISTEM (courtesy of F. Guglielmino; INGV copyright).

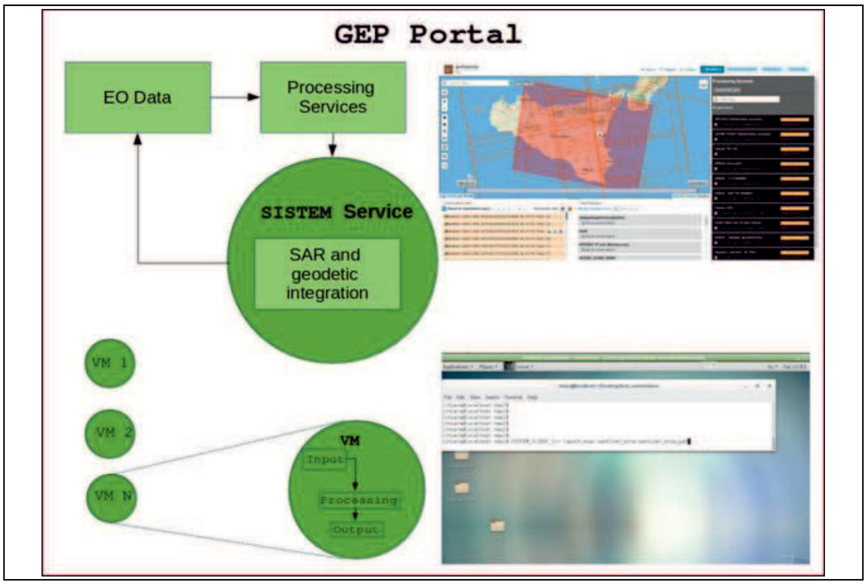

Figure 21
The SISTEM service integration on the GEP Platform. Users can submit data discovery queries, visualize several different EO Data sources (different satellite missions, periods, orbits, area, etc.), and analyse them by using the GEP Processing Services. SISTEM software is one these GEP processing services. Bottom right: users can create their own VM to process their data with SISTEM Software in an independent fashion (courtesy of F. Brito; T2 copyright).

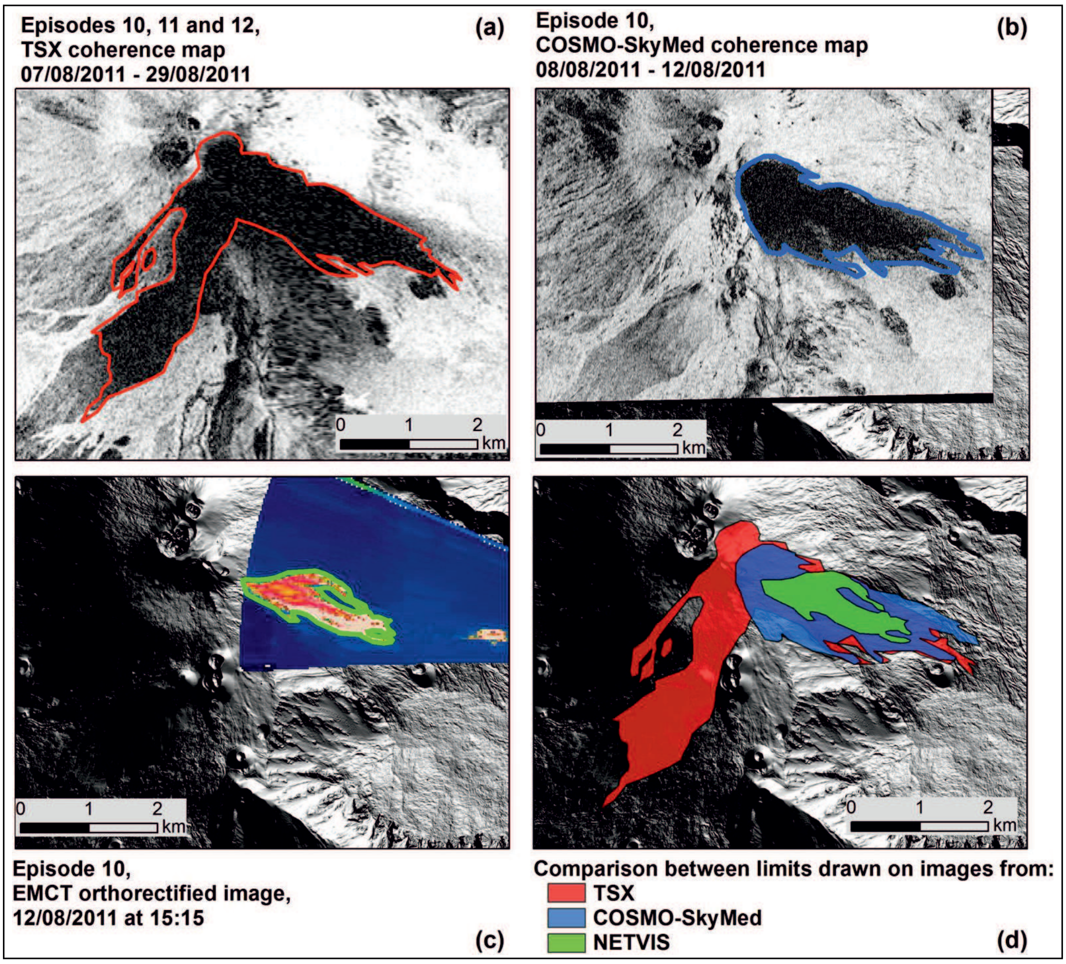

Figure 22
Integration of the SAR images (TSX and CSK) and NETVIS results: (a) low coherence values delimited on the 07/08/2011-29/08/2011 TSX map; (b) low coherence values delimited on the 08/08/2011-12/08/2011 CSK map; (c) lava flow limits drawn on the 12/08/2011 EMCT orthophoto; (d) comparison between the three limits. Coherence values from low to high are represented as colours from black to white in panels (a) and (b) (courtesy of M. Marsella; SurveyLab copyright).

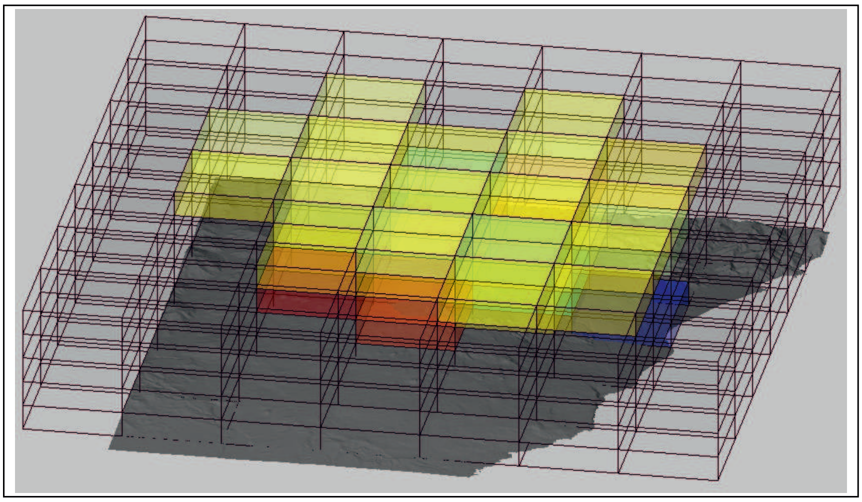

Figure 23
EO and in-situ data Integration: 3D Tomography (ppm) during the Sentinel-1 pass on 2015 obtained by integrating GPS and satellite data (courtesy of M. Aranzulla; INGV copyright).

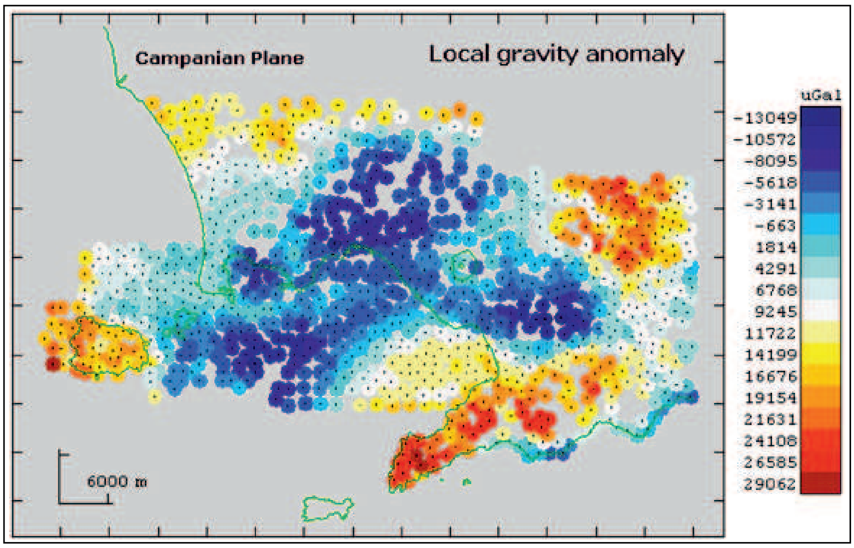

Figure 24
New constraints on the structure of the Neapolitan volcanoes: Local anomaly obtained by removing the adjusted regional trend from the observed gravity anomaly in the Campania Plane; (courtesy of J. Fernandez; CSIC copyright).

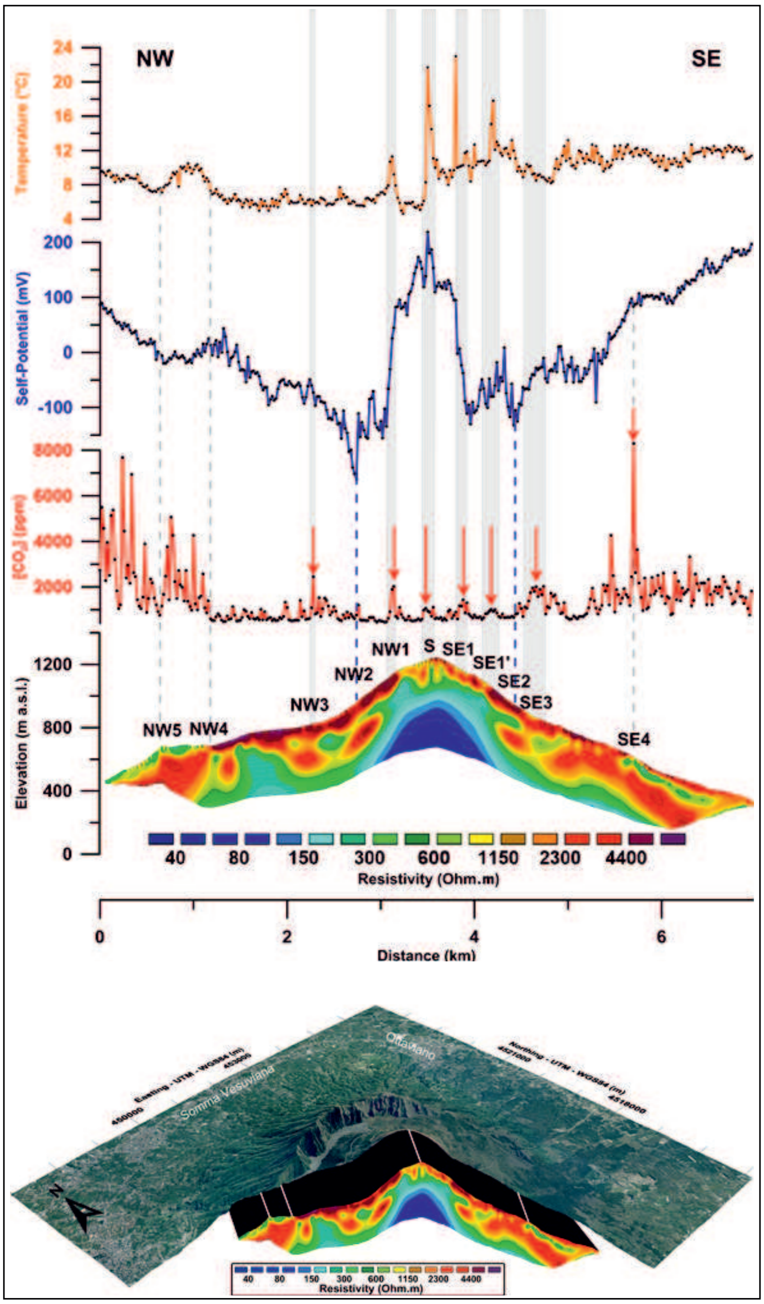

Figure 25
New constraints on the structure of Somma-Vesuvius: (top) NW-SE profile of DC electrical resistivity tomography, self-potential, soil degassing and sub-surface temperature crossing the volcano; preliminarily results. (bottom) 3D view of the Somma-Vesuvius area showing the NW-SE 2D cross section and the results of the DC electrical resistivity tomography; (courtesy of A. Finizola; CNRS copyright).

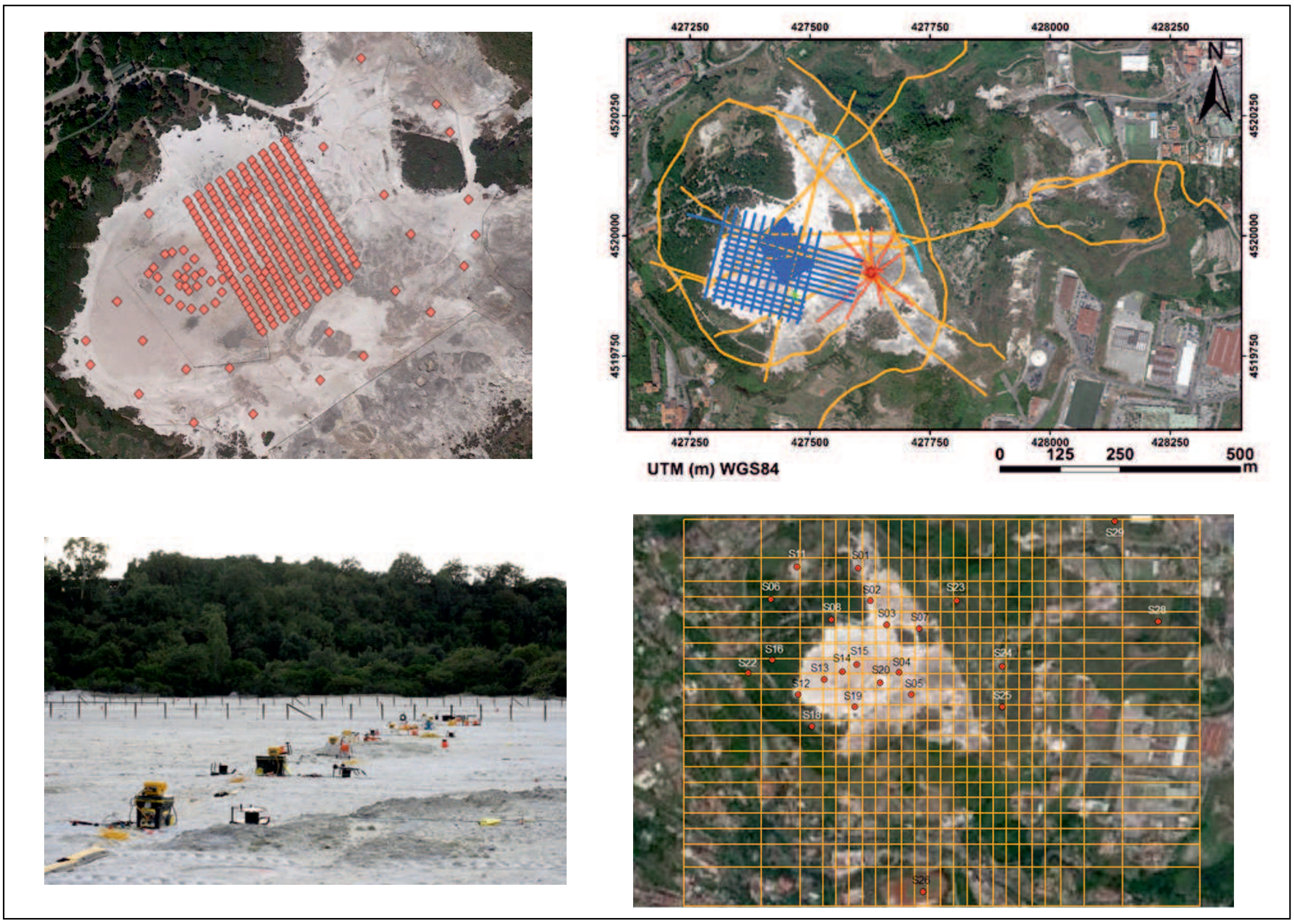

Figure 26
New constraints on the structure of the Neapolitan volcanoes: Geophysical surveys in the Solfatara - Pisciarelli area: a) Position of the stations during the RICEN experiment; b) View of the instrumentation used for the 3D experiment installed in front of the Fangaia area (courtesy G. Festa; AMRA copyright); c) Map of the Solfatara-Pisciarelli area showing the ERT profiles. Long profiles (960 and 1200 m long) are shown in orange, high-resolution radial short-profiles in the fumarolic area (shown in red), and high-resolution profiles in the Fangaia mud pool area (in blue). The time-lapse resistivity profile on the eastern flank of Solfatara is shown in light blue (courtesy of J. VandemelbroucK; CNRS copyright); d) Location of the AMT soundings used for modelling and inner spacing grid of the 3D model (courtesy of A. Siniscalchi; AMRA copyright).

Figure 27
New constraints on the structure of Somma-Vesuvius: results of the geophysical surveys at La Sofatara crater: S wave velocity model as obtained from inversion of surface waves, compared to the model obtained for the resistivity; (courtesy of G. Festa; AMRA copyright).

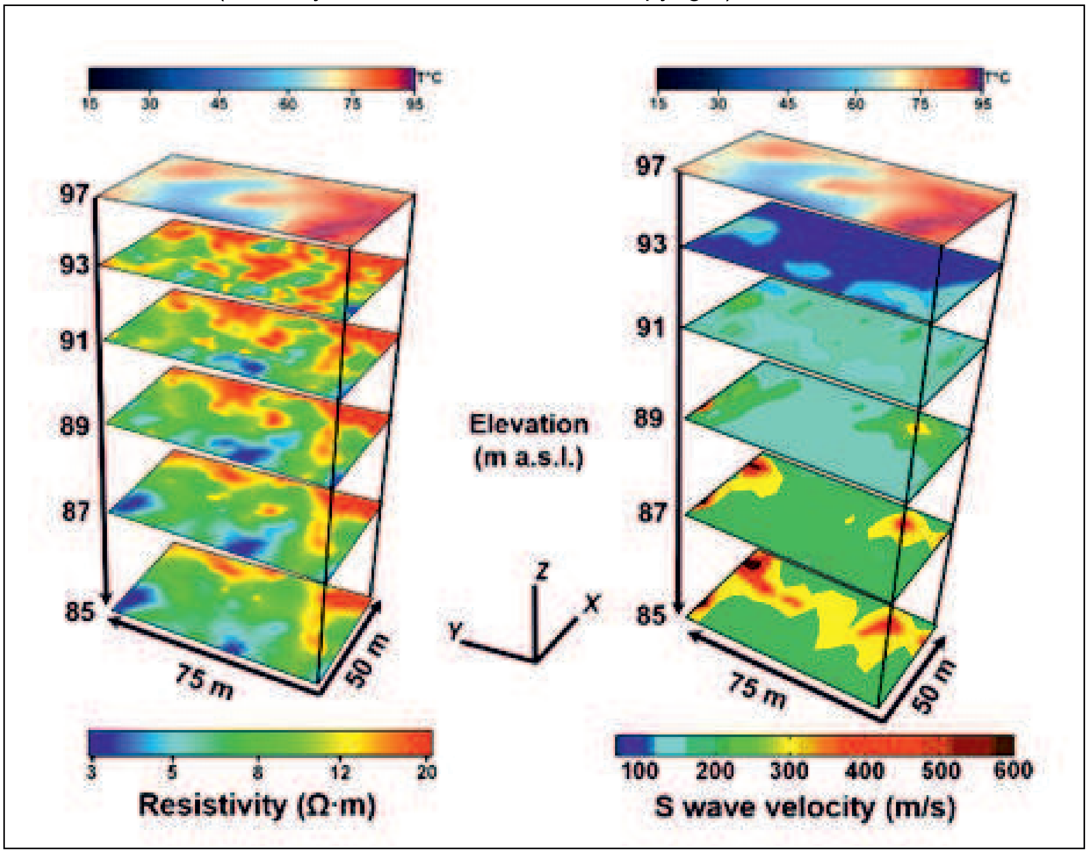

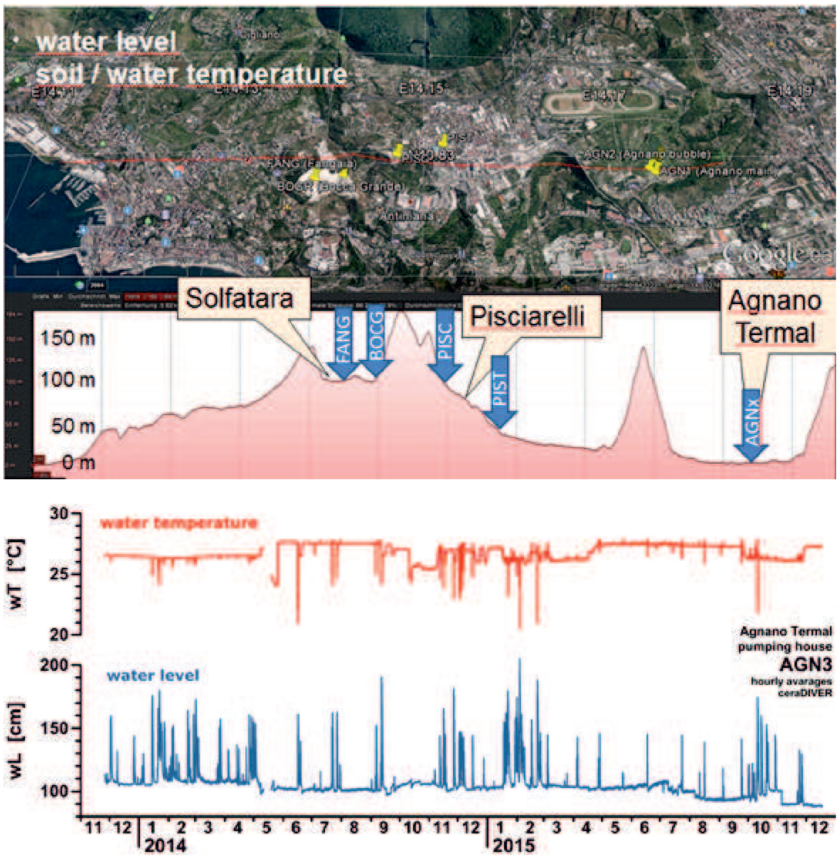

Figure 28
Improvements on the hydrothermal system at Campi Flegrei: surveys for studying pressure transients in fluid reservoirs (courtesy of H, Woith; copyright GFZ).
(top) Location of continuous fluid monitoring sites in Campi Flegrei; (bottom) Agnano pumping house (AGN3) water level and water temperature; water level has been corrected with barometric data from AGN3baro. Shown are hourly averages.

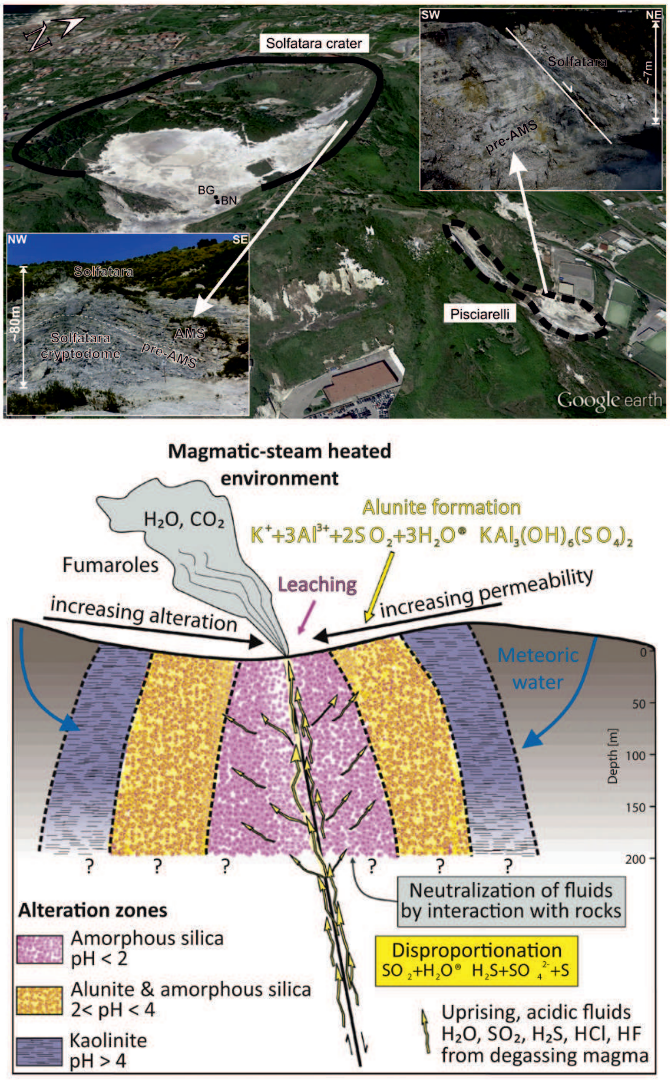

Figure 29
Improvements on the hydrothermal system at Campi Flegrei: study on the hydrothermal alteration of surficial rocks at Solfatara (Campi Flegrei): petro-physical properties and implications for phreatic eruption processes.
(top) Google Earth™ image of Solfatara crater and Pisciarelli fumarole. Insets show the details of the locations of the samples;
(bottom) conceptual model for the formation of near surface high-sulfidation alteration. Fuid temperature, pH and composition control the development of alteration zones in relation to the distance to main fumarolic conduit. A highly permeable, acidic core characterized by amorphous silica is laterally replaced by a zone of alunite and amorphous silica. Successive neutralization of the fluids promotes the formation of kaolinite. Rock permeability as well as the degree of alteration increase toward the center of the hydrothermal activity (Mayer, K. et al., J. Volcanol. Geoth. Res., 2016).

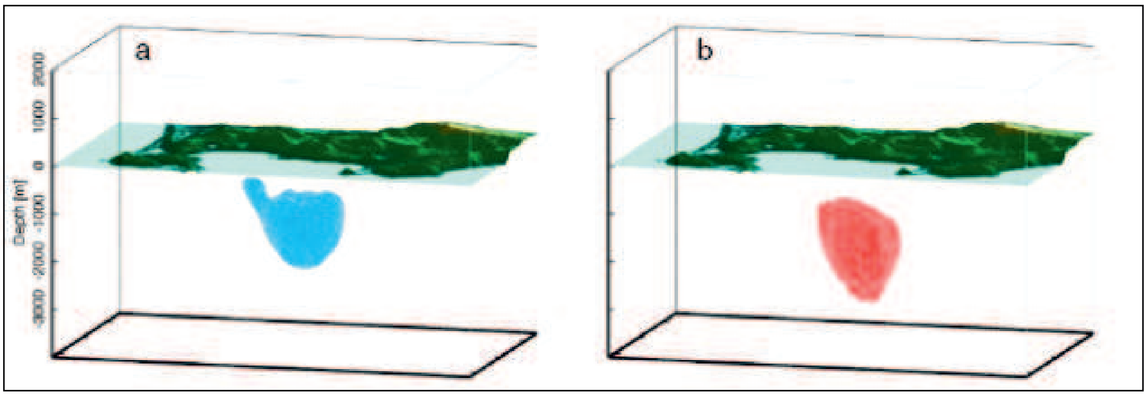

Figure 30
Simultaneous joint inversion of SAR and GPS data a) Three-dimensional location and shape of deflation source model for the period 1993–1999; (b) three-dimensional location and shape of inflation source model for the period 2007–2013 (Samsonov et al., 2014).

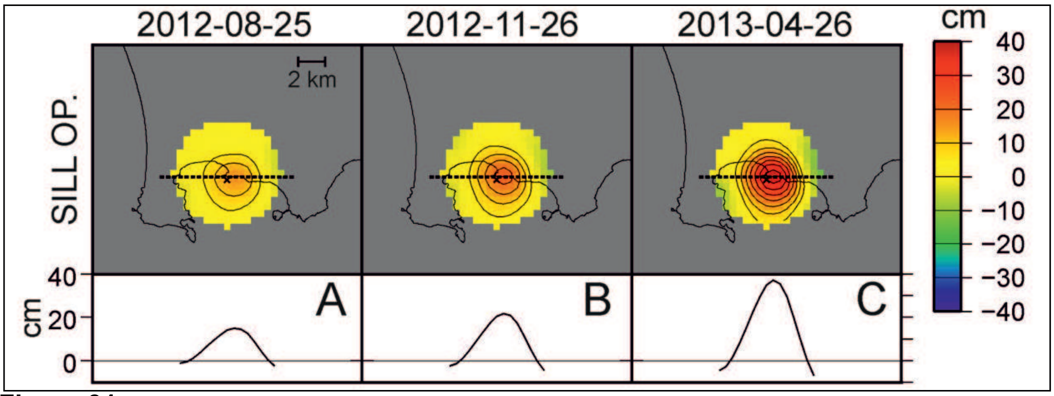

Figure 31
Results of the geodetic imaging for three selected intervals of the 2012-2013 unrest. The cross represents the point of coordinates (14.20°E 40.82°N). A, B, C) Opening of the sill (at 3100 m depth). Map of the sill opening are shown on top of each panel. Contours spacing is 5 cm. On the bottom we represent the opening along the profiles marked by dashed lines.

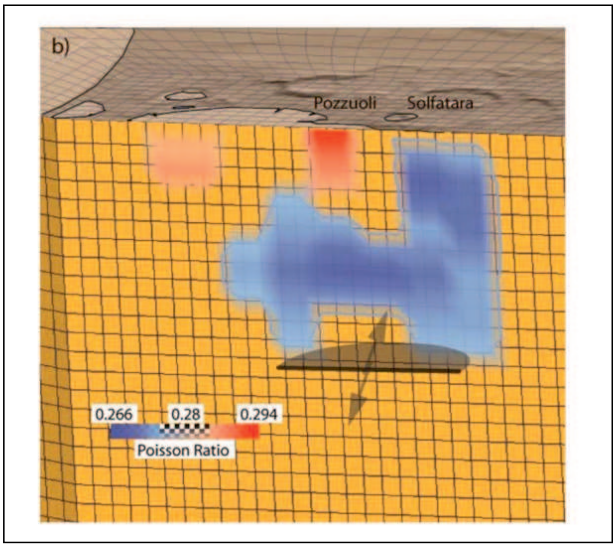

Figure 32.
Sketch of the unrest ground deformation source within the FE model (from Trasatti et al., 2015).

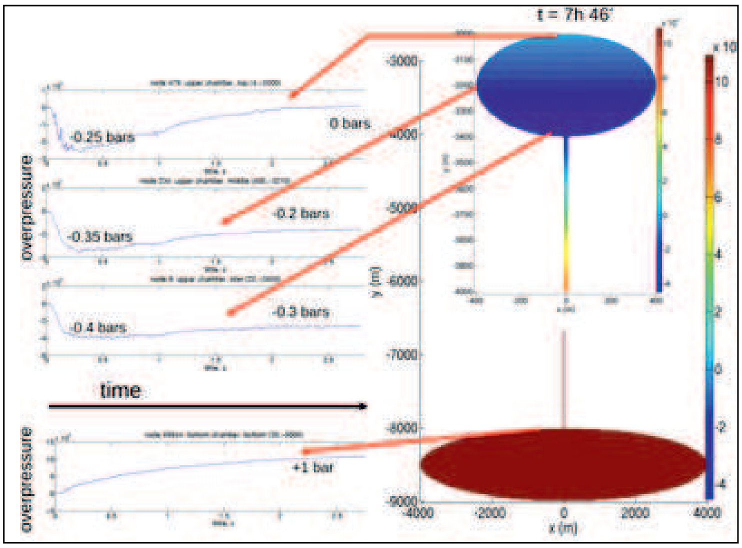

Figure 33
Pressure evolution in space and time in a two-chamber system. Left panel: time series of pressure at selected points in the domain, indicated by the arrows. Right panel: snapshot of overpressure, with respect to the initial magma-static distribution, after about 8 hours of simulated time, in the upper and lower portions of the domain, showing depressurization at the top and pressurization at the bottom (courtesy of P. Papale, INGV copyright).

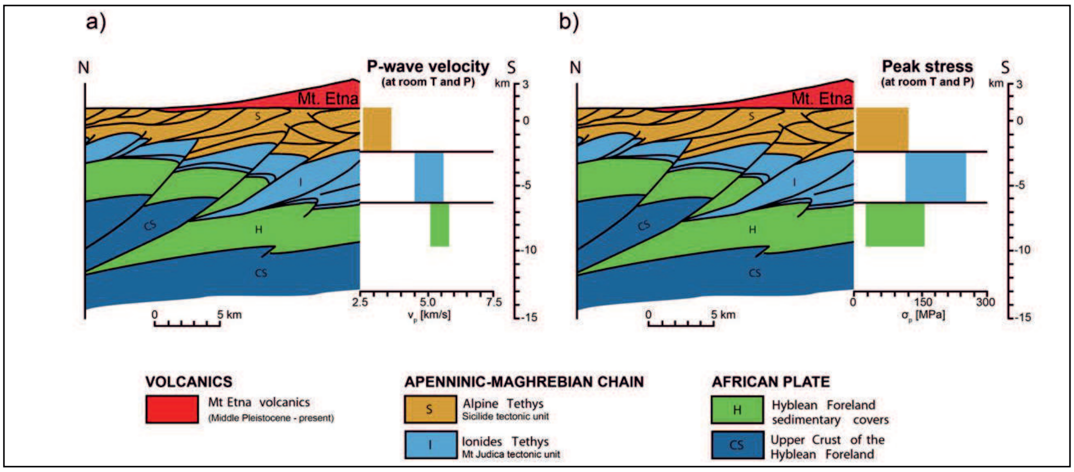

Figure 34
New constraints on the structure of Mt. Etna volcano. (1) Variability of laboratory experimental data in correlation with stratigraphic position of rock units. a) p-wave velocity and b) uniaxial compressive strength. (Wiesmaier et al., J. Volcanol. Geoth. Res., 2015).

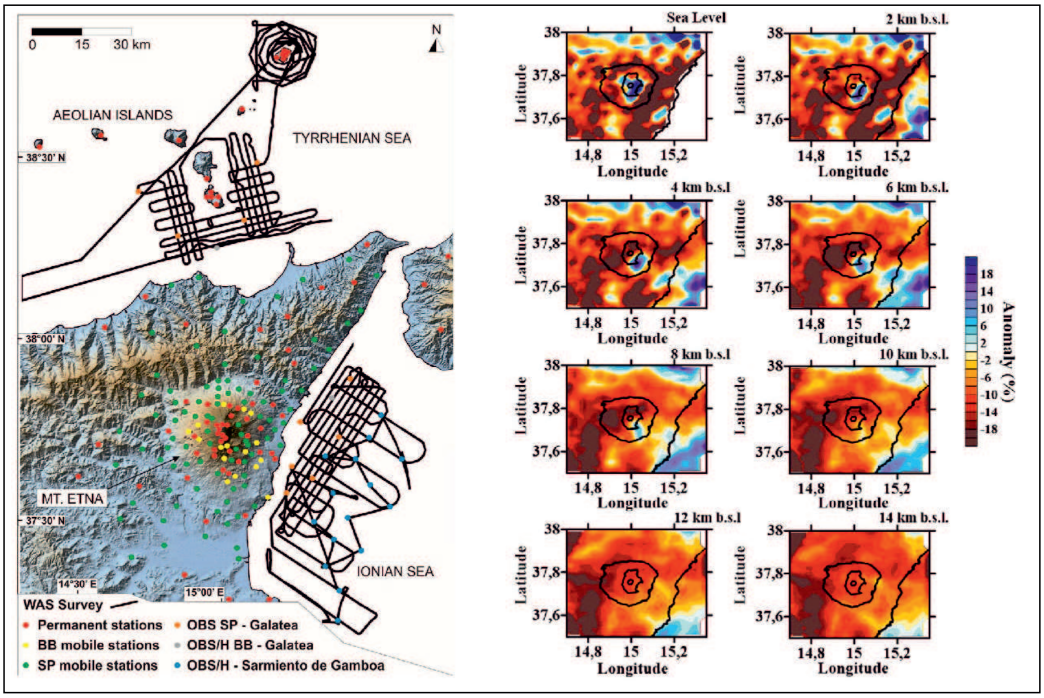

Figure 35
New constraints on the structure of Mt. Etna volcano. (left) Lines of shots and location of the seismic station of TOMO-ETNA experiment; (right) first TOMO-ETNA identified anomalies in the velocity structure (courtesy of J. Ibanez; UGR copyright).

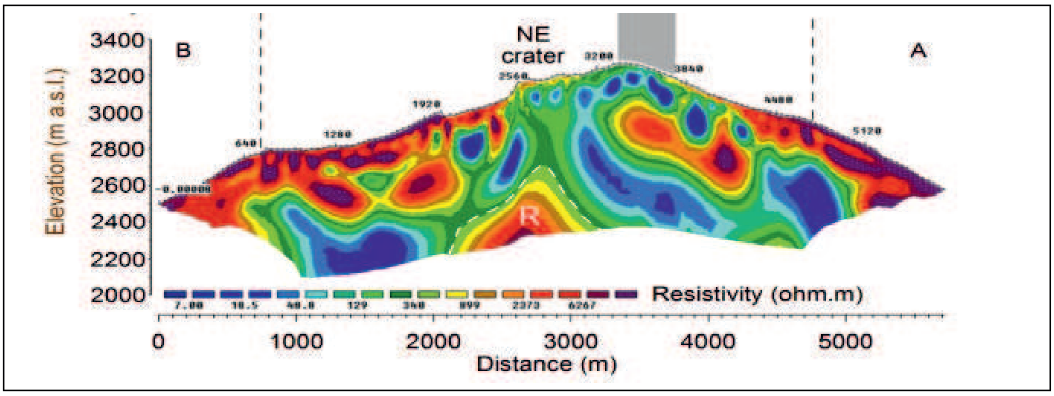

Figure 36
New constraints on the structure of Mt. Etna volcano. Electrical Resistivity Tomography profile crossing the North East Crater (courtesy of A. Finizola; CNRS copyright).

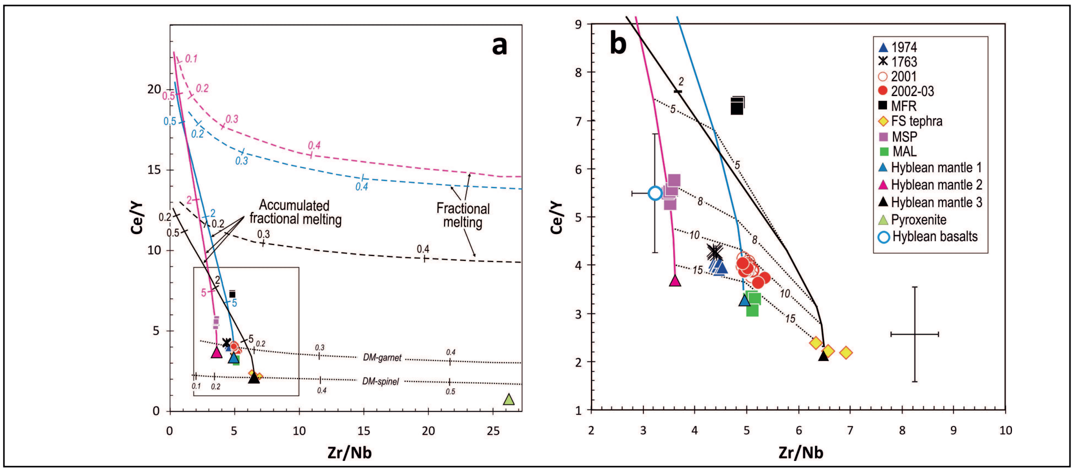

Figure 37
Improvements on Mt. Etna plumbing system. Ce/Y vs. Zr/Nb of Etna ‘deep-dyke fed’ basalts. a) Curves of non-modal fractional melting (dashed lines) and accumulated fractional melting (continuous line) are plotted for three Hyblean-type mantle sources. Ticks indicate different percentages of melting. The curves of fractional melting for depleted garnet and spinel mantles are provided for comparison (dotted grey lines). b) Enlargement of the grey area in Figure a, showing exclusively the curves for accumulated fractional melting of Hyblean-type mantle sources suitable for Mt Etna, with dotted isolines of melting percentages. (Corsaro and Métrich, Lithos, 2016).

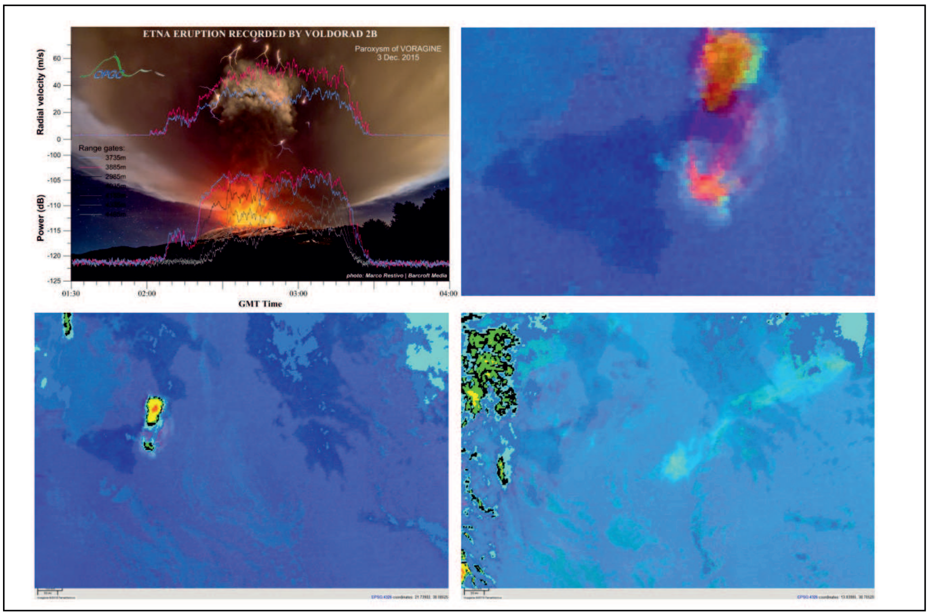

Figure 38
Improvements on Mt. Etna plumbing system. Example of radar (VOLDORAD 2B) near source monitoring of lava fountain and MSG-SEVIRI satellite tracking of the tephra plume and distal cloud of Voragine on Dec. 3 2015. (Top left); (Top right) HOTVOLC RGB image at 06:00 UTC. Bottom: HOTVOLC SO2 product showing tephra plume over East Sicily at 06:00 UTC (left) and 17:45 UTC (right). HOTVOLC open data base at http://hotvolc.opgc.fr/hotvolc/fr/ (courtesy of Donnadieu; UBP-LMV copyright).

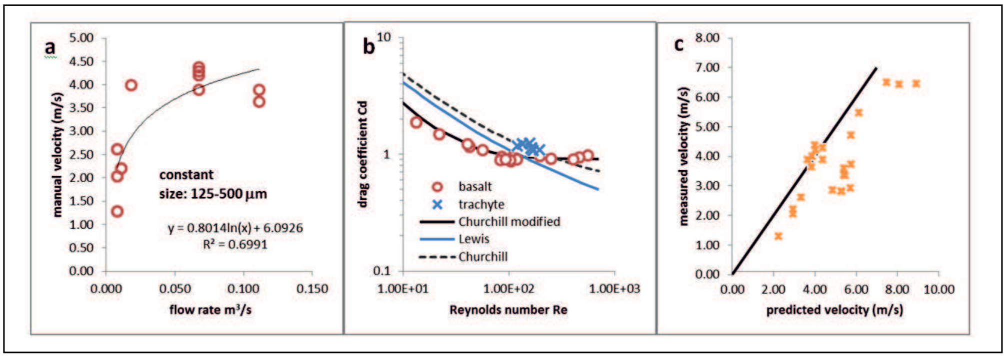

Figure 39
Improvements on Mt. Etna plumbing system. Results of high-speed imaging tracking analyses to characterize particle settling dynamics as a function of particle concentration in the flow, density and particle size (courtesy of P. Scarlato; INGV copyright).

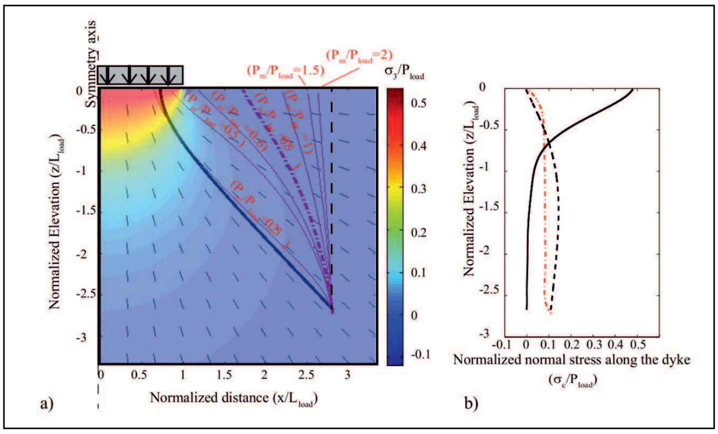

Figure 40
Improvements on Mt. Etna Dynamics. Dyke trajectories in a crust loaded at the surface for a dike starting at a normalized depth of 2.7 and a normalized radial distance of 2.8 from the axis of the load (courtesy of E. Rivalta; GFZ copyright).

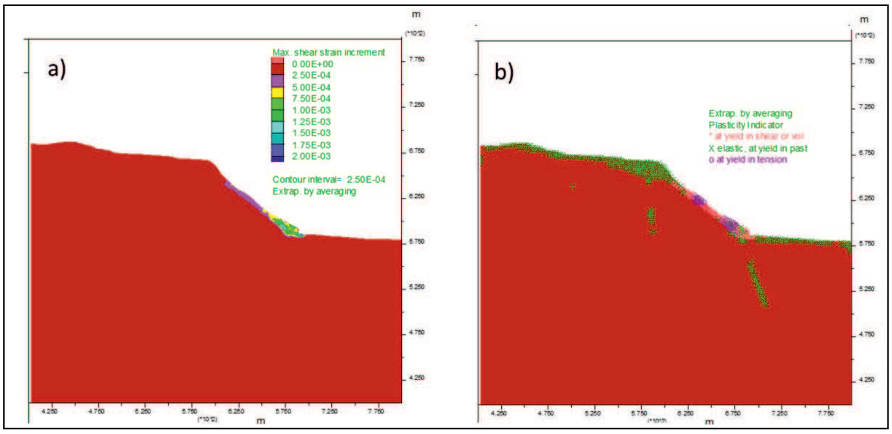

Figure 41
Improvements on Mt. Etna Dynamics. Results of stress-strain analysis of the Presa - Vena area (a) maximum shear strain increment at the elasto-plastic equilibrium and dry condition (courtesy of T. Apuani; UNIMI copyright).

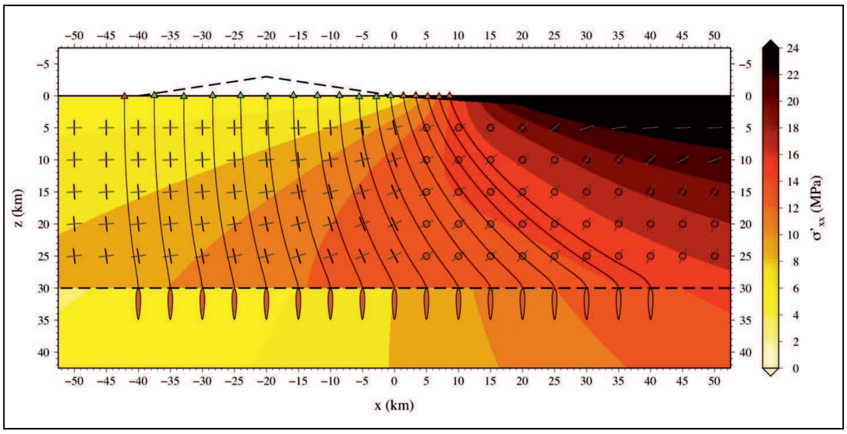

Figure 42
Improvements on Mt. Etna Dynamics. Dike trajectories are influenced by the loading/unloading due to the Malta Escarpment (courtesy of E. Rivalta; GFZ copyright).

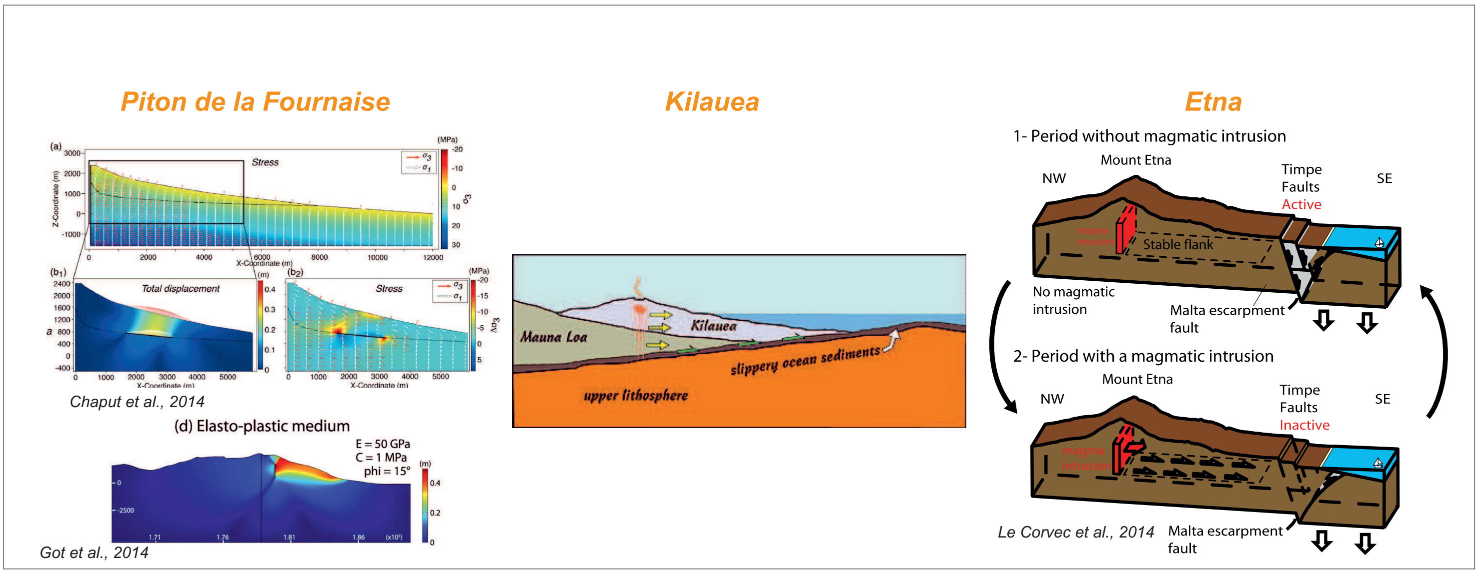

Figure 43
Improvements on Mt. Etna Dynamics. Comparison of flank dynamics at basement setting and volcanic activity and stability at three Supersite volcanoes: Etna (Sicily, Italy), Kilauea (Island of Hawaii, USA) and Piton de la Fournaise (La Reunion Island, France) (courtesy of A. Bonforte; INGV copyright).

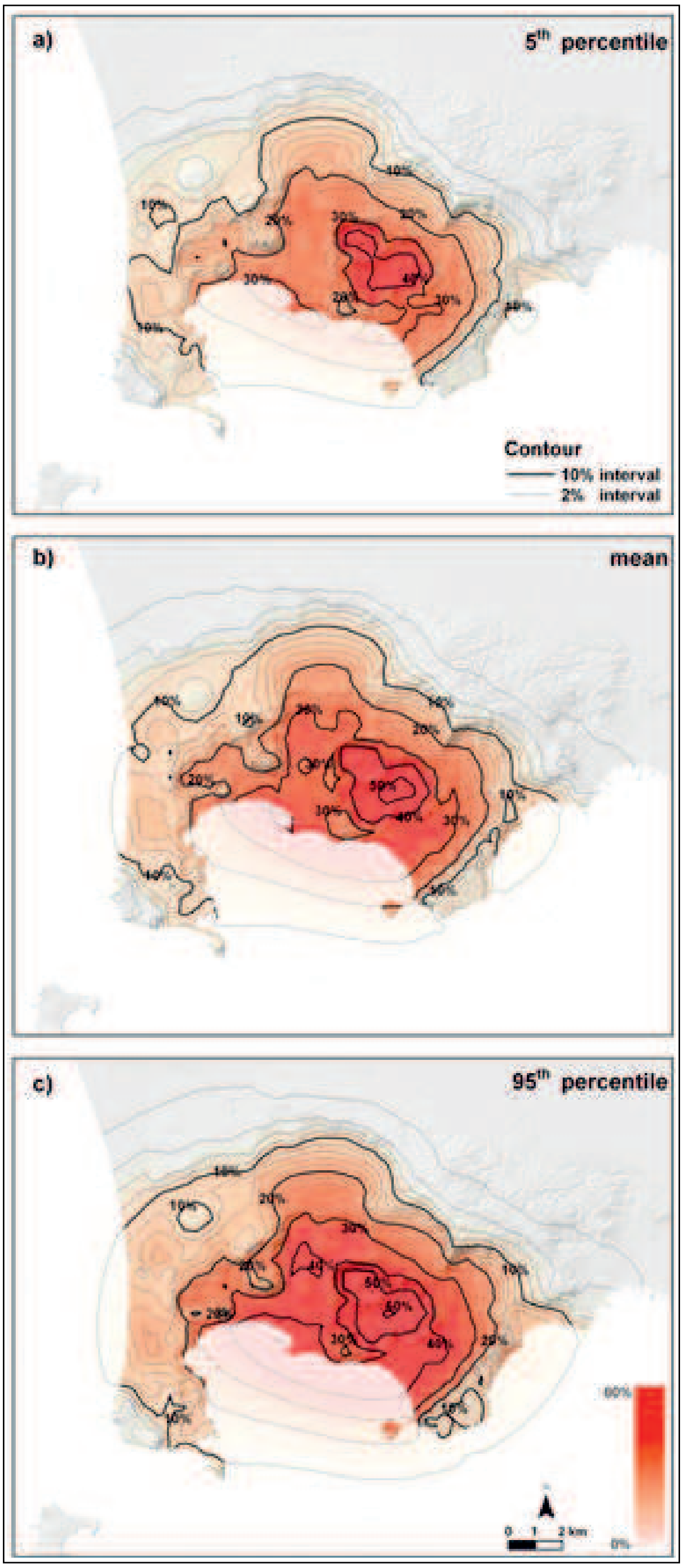

Figure 44.
Pyroclastic density current invasion maps of Campi Flegrei caldera as presented in Neri et al. [2015]. The three maps refer to the 5th, mean and 95th percentile of the distribution.

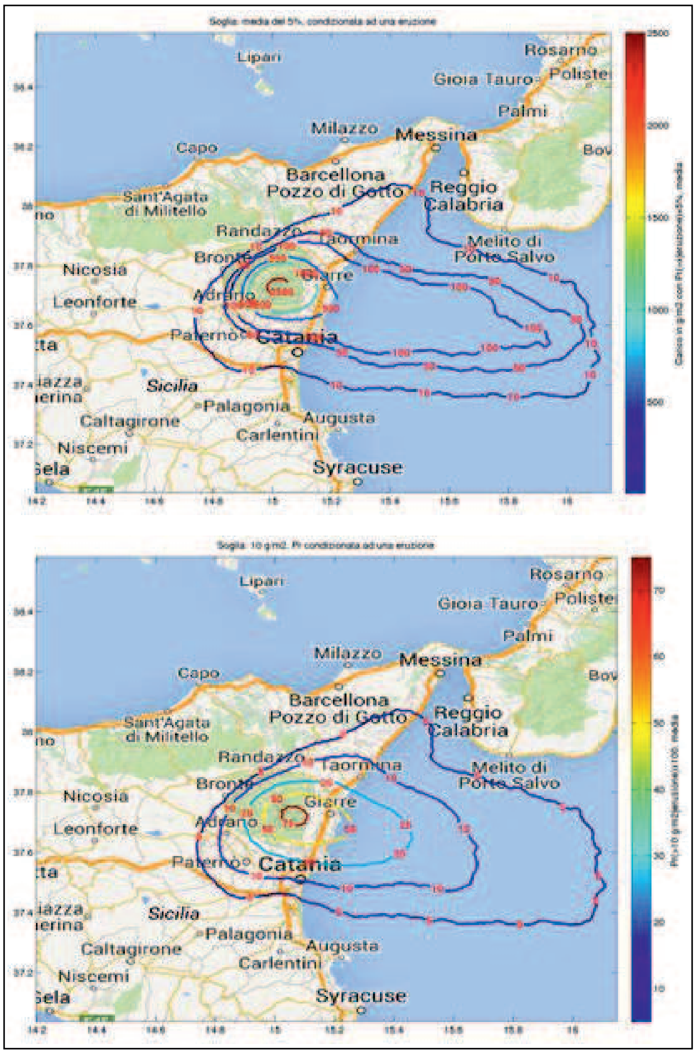

Figure 45.
Tephra fall hazard results for summit eruptions, considering the mean of the epistemic uncertainty. The results are reported as (upper panel) hazard map relative to a threshold of 5% of the probability exceedance, conditioned to the occurrence of a summit eruption, and (bottom panel) the probability map of exceeding 10 g/m2, given a summit eruption.